RARE METALS

ORIGINAL ARTICLE

Melting mechanisms of Pt-based multimetallic spherical nanoparticles by molecular dynamics simulation

Chun-Yu Cheng, Yuan-Yuan Guo, Yi-Ming Zou, Amanda Jiamin Ong,
Alfred Iing Yoong Tok* , **Shuzhou Li***

Abstract The melting mechanisms of Pt-based multimetallic nanoparticles (NPs) are important to help determine their optimal melting processes. To understand the melting and coalescence behaviors of heterogeneous NPs (Pd–Pt NPs) with various sizes and compositions, molecular dynamics (MD) simulation was employed. The MD results for larger Pd–Pt NPs with an effective diameter of 4.6–7.8 nm show that PtPd alloy can form at Pd/Pt interface before Pd NP melted completely, while for Pt-core/Pd-shell NP and Pd-core/Pt-shell NP, PtPd alloy formed only after Pd portion melted completely. For smaller Pd–Pt NPs with an effective diameter of 2.5–4.0 nm, PdPt alloy is not formed until both Pd and Pt NPs melted completely. Besides, the coalescence process of Pd–Pt NPs depends on the melting temperature of Pt NP when Pt composition is higher than 20 at%. Furthermore, the melting mechanisms of Pd/Pt/Ir trimetallic NPs are investigated. A two-step melting process occurs in Pd–Pt–Ir NPs and Ir-core/Pt-shell/Pd-shell NP, and the melting sequence of Pd-core/Pt-shell/Ir-shell NP and Pt-core/Pd-shell/Ir-shell NP is different from Pd/Pt bimetallic NPs.

Keywords Molecular dynamics (MD); Melting mechanism; Pt-based; Multimetallic; Heterogeneous structure

C.-Y. Cheng, Y.-Y. Guo, Y.-M. Zou, A. J. Ong,
A. I. Y. Tok*, S. Li*
School of Materials Science and Engineering, Nanyang Technological University, Singapore 639798, Singapore
e-mail: MIYTok@ntu.edu.sg

S. Li
e-mail: lisz@ntu.edu.sg

1 Introduction

Due to its excellent stability and high catalytic activity, Pt is widely used in many applications, such as the chemical industry and the petrochemical industry [1–6]. The scarcity of Pt, however, limits its application on a large scale. To reduce the amount of Pt while maintaining its catalytic activity, an effective way is to use Pt-based multimetallic nanoparticles (NPs) with a high density of active sites [7–12]. Among them, Pd/Pt bimetallic NPs are widely studied and have shown excellent properties in oxygen reduction reactions, ethanol oxidation reactions, and methanol oxidation reactions [13–17]. Up to now, Pd/Pt bimetallic NPs have been synthesized by many technologies operating at room temperature, such as solvothermal route [18, 19], atomic layer deposition [20], seed-mediated growth [21, 22], and seedless wet-chemical approaches [23]. The former method prepares heterogeneous Pd–Pt NPs (Pd–Pt NPs) where each NP is adjacent to each other, and the latter three fabricate core–shell structures with one NP being enveloped by the other, including Pt-core/Pd-shell NP (Pt@Pd NP) and Pd-core/Pt-shell NP (Pd@Pt NP). Since these NPs need to be alloyed at high temperatures to control their catalytical properties, several attempts have been made to understand their melting mechanisms under the heating process by molecular dynamics (MD) simulations [24–26].

MD simulations [24–26] have shown that the melting of Pt@Pd NPs with a diameter of 6.2 nm started from Pd shell to Pt core, and occurred over a broad range of temperatures. Unlike Pt@Pd NP, a fast-melting process emerged in Pd@Pt NP with the same diameter due to an instantaneous transition of the solid–liquid phase of Pd core. Nelli et al. [27] investigated the coalescence of (Pt–Pd)@Pd NPs and

focused on the change in the shape of (Pt–Pd)@Pd NPs. They found that the coalescence process occurred through four different steps, consisting of the alignment of atomic columns, alignment of close-packed atomic planes, equilibration of shape, and equilibration of chemical ordering. In recent years, Pd–Pt NPs consisting of one or more Pd NPs and Pt NPs with a diameter of 2–10 nm have been applied in the industry [18, 28, 29]. However, their melting processes have not been studied, which might be different from the melting processes of core–shell NPs due to the various specific surface area as well as structures. And in addition to the change of shape, the change of the NPs' composition is also a matter of concern, which has not been deeply studied by Nelli et al. [27]. Since the catalytic activity of nanocatalysts is strongly affected by their size and surface atoms, the effect of heat treatment on the sizes and surface atoms is also important to prepare these highly active nanocatalysts. Furthermore, Pd/Pt/Ir multimetallic NPs have also been used in catalysis fields because they possess higher catalytic activity than the commercial Pt/C NP for oxygen reduction and evolution reactions [30]. It is also important to understand their melting processes.

In our current study, we first focused on a systematic study on the melting and coalescence processes of Pd–Pt NPs by MD simulation and compared these to the melting mechanisms of Pd@Pt and Pt@Pd NPs. MD results show that the disordered PdPt alloy appeared at the interface before Pd NP has completely melted in larger Pd–Pt NPs with the effective diameter of 4.6–7.8 nm, and it is propagated into the interior of both Pd and Pt NP. This process is different from the melting processes of the Pd@Pt and Pt@Pd NPs, where no disordered PdPt alloy is obtained at the interface before the Pd portion has completely melted. Moreover, smaller Pd–Pt NPs with an effective diameter of 2.5–4.0 nm exhibit a distinct coalescence process, where the alloyed PdPt is only obtained after both Pd NP and Pt NP have completely melted. The melting mechanisms of Pd/Pt/Ir trimetallic NPs, including Pd–Pt–Ir NPs with one Pd NP, one Pt NP, and one Ir NP, Pd-core/Pt-shell/Ir-shell NP (Pd@Pt@Ir NP), Pt-core/Pd-shell/Ir-shell NP (Pt@Pd@Ir NP), and Ir-core/Pt-shell/Pd-shell NP (Ir@Pt@Pd NP) are also investigated. The coalescence process of Pd–Pt–Ir NPs and Ir@Pt@Pd NP exhibits two stages because the melting temperature of Ir portion is higher than the other two parts. The melting process of Pd@Pt@Ir NP and Pt@Pd@Ir NP starts in the two outermost layers. Hence, the melting processes of Pd/Pt/Ir trimetallic NPs are different from those of Pd/Pt bimetallic NPs. When the melting points of the three compositions in the trimetallic NPs are significantly different, the trimetallic NPs will experience a two-stage melting process instead of one uniform melting process.

2 Computational details

Large-scale atomistic/molecular massively parallel simulator (LAMMPS) [31, 32] was employed to study the melting mechanisms of Pd/Pt bimetallic NPs, including Pd–Pt NPs, Pd@Pt NP, and Pt@Pd NP, as displayed in Fig. 1a. Pt composition in each NP was set at 50 at%. The number of atoms varied from ∼ 660 to ∼ 16,800. The cell size was fivefold the longest size of the constructed model. To facilitate the comparison of NPs with the same number of atoms but different structures, the effective diameter (d_{ED}) of Pd–Pt NPs was defined as below:

$$d_{ED} = 2 \times \sqrt[3]{\frac{3(V_{Pd} + V_{Pt})}{4\pi}} \quad (1)$$

where V_{Pd} and V_{Pt} are the volumes of Pd NP and Pt NP in Pd–Pt NPs, respectively. Besides, Pt composition was varied from 10 at% to 80 at% to explore the effect of Pt composition on the melting and coalescence mechanisms of Pd–Pt NPs with a d_{ED} of 6.3 nm. The number of atoms and diameter of Pd–Pt NPs and core–shell NPs are provided in Table 1 and Table S1, respectively. To study the melting mechanisms of Pd/Pt/Ir trimetallic NPs, Pd–Pt–Ir NPs, Pd@Pt@Ir NP, Pt@Pd@Ir NP and Ir@Pt@Pd NP were also built, as shown in Fig. 1b. The ratio of the number of Pd, Pt and Ir atoms was set at 1:1:1 where the number of atoms was 9189. d_{ED} of Pd–Pt–Ir NPs was defined as below:

$$d_{ED} = 2 \times \sqrt[3]{\frac{3(V_{Pd} + V_{Pt} + V_{Ir})}{4\pi}} \quad (2)$$

where V_{Ir} is the volume of Ir NP in Pd–Pt–Ir NPs. The number of atoms, the thickness of the shell, and the diameter of the four types of Pd/Pt/Ir trimetallic NPs are displayed in Table 2.

The embedded atom method (EAM) potential [33] was used to describe the interatomic potential for the Pd, Pt and Ir. A mixing rule reported by Johnson [34] was employed to construct an EAM potential for the alloyed Pd–Pt–Ir system. The potentials were evaluated through the
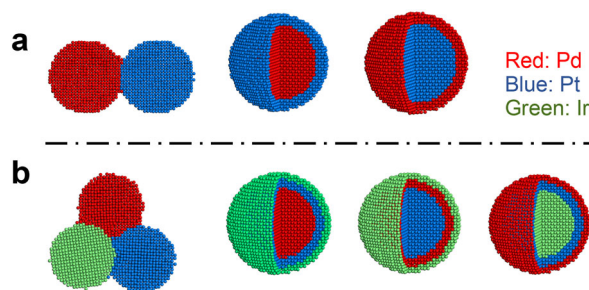

Fig. 1 Initial configurations of **a** Pd/Pt bimetallic NPs and **b** Pd/Pt/Ir trimetallic NPs

Table 1 Number of atoms and diameter of Pd–Pt NPs

Number of atoms	Pt composition / at%	Diameter of Pd NP / nm	Diameter of Pt NP / nm	d_{ED} of Pd–Pt NPs / nm
658	50	2.0	2.0	2.5
1268	50	2.6	2.6	3.2
2288	50	3.2	3.2	4.0
3830	50	3.8	3.8	4.8
6106	50	4.4	4.4	5.5
9046	50	5.0	5.0	6.3
12,852	50	5.6	5.6	7.0
16,804	50	6.2	6.2	7.8
9046	10	3.0	6.1	6.3
9046	20	3.7	5.9	6.3
9046	80	5.9	3.7	6.3

Table 2 Number of atoms, thickness of shell, and diameter of four types of Pd/Pt/Ir trimetallic NPs (diameter of each NP in Pd–Pt–Ir NPs being 4.3 nm)

Parameters	Pd–Pt–Ir NPs	Ir@Pt@Pd NP	Pd@Pt@Ir NP	Ir@Pd@Pt NP
Number of atoms	9189	9189	9189	9189
Diameter or effective diameter of NP(s) / nm	6.3	6.3	6.3	6.3
Thickness of outmost shell / nm	–	0.4	0.4	0.4
Diameter of core / nm	–	4.3	4.3	4.3

thermodynamic properties of metals and their alloys, which are shown in the Supporting Information.

The total energy (E) of the EAM potential was written as:

$$E_i = F_i \sum_{i \neq j} \rho_{ij} r_{ij} + \frac{1}{2} \sum_{i \neq j} U_{ij} r_{ij} \tag{3}$$

where E_i and F_i are the cohesive and embedding energies of i atom, respectively. $\rho_{ij} r_{ij}$ is the electron density of j atoms located around i atom at a distance r_{ij}. F_i is a many-body interaction term, while U_{ij} takes the pair interaction into account. The melting point of bulk Pd of the EAM potential is (1827 ± 15) K, which is well consistent with the experimental result (1828 K). Thus, the EAM potential describes the melting process of Pd accurately. The melting points of bulk Pt and Ir of the EAM potential are (1890 ± 15) and (2280 ± 15) K, respectively, which is in good agreement with the simulated results (1890 and 2280 K, respectively) [33], and only qualitatively agree with the experimental values (2041 and 2739 K, respectively).

At the start of the MD simulation, all the constructed NPs were first relaxed to a minimum energy state by iteratively adjusting atom coordinates [31, 32]. After relaxation, the NPs were heated using a certain algorithm-thermostats. The most adequate in the task on the determination of thermal stability of NPs was the Nosé–Hoover thermostat. Herewith, the number of particles N, the volume V of a space simulated, and the temperature T were assumed to be constant, which gives a so-called NVT ensemble. The heating rate of these NP systems was 0.5 K·ps^{-1}, and the time step was 1 fs. A series of MD simulations were performed with an increment of 100 K from 0 to 2000 K. In addition, an increment of 20 K was used around the melting point to investigate the melting mechanism in detail. Starting from 0 K, the system temperature was increased by 10 K within 20 ps. After reaching the set temperature, the system was equilibrated by 1000 ps at a constant temperature. These heating and equilibrium processes were repeated until the NP completely melted. The output value of each physical quantity was obtained from the statistical average value in the last 100 ps of the equilibrium process.

Lindemann index, a commonly used method to describe the thermally driven disorder of a system, was calculated to characterize the melting process of the NPs [24–26].

Lindemann index (δ_i) was defined as the root-mean-square bond fluctuation [35]:

$$\delta_i = \frac{2}{N(N-1)} \sum_{i<j} \frac{\sqrt{\langle R_{ij}^2 \rangle - \langle R_{ij} \rangle^2}}{\langle R_{ij} \rangle} \quad (4)$$

where N is the number of atoms and R_{ij} is the distance between i and j atoms. The brackets $\langle\ \rangle$ are the ensemble average at the given temperature. Since the surface atoms affect the melting process of NP, the melting of NP occurs when the value of the Lindemann index is in the range of 0.03–0.05, depending on the diameter of NP [35].

The radial distribution function (RDF) was employed to investigate the structural evolutions of NPs during the heating process. The RDF of B atom in the distance (r) from A atom ($g(r)$) was calculated by [36]:

$$g(r) = \frac{\langle n(r) \rangle}{4\pi r^2 \mathrm{d}r \rho_A N_B} \quad (5)$$

where $n(r)$ is the number of B atoms between r and $r + \mathrm{d}r$. $4\pi r^2 \mathrm{d}r$ is the volume. ρ_A denotes the number density of A atom in the system. N_B is the total number of B atoms in the system.

3 Results and discussion

3.1 Melting and coalescence processes of Pd–Pt NPs

The Lindemann indices of Pd–Pt NPs, Pt@Pd NP and Pd@Pt NP with d_{ED} or diameter (d) of 6.3 nm as a function of the temperature are shown in Fig. 2a. Lindemann index curves of the three types of Pd/Pt bimetallic NPs rise linearly as the temperature increase at low temperature and subsequently present a jump when the transition from solid to liquid, which indicates the NPs are completely melted. A broad Lindemann index rise (black arrow in Fig. 2a) appears in Pd–Pt NPs and Pt@Pd NP, unlike the sharp Lindemann index jump in Pd@Pt NP.

To track the melting and coalescence process of Pd–Pt NPs with d_{ED} of 6.3 nm during the heating process, the snapshots of the cross section taken at four representative temperatures are displayed in Fig. 2b. Figure 2c shows the RDF of Pd–Pt NPs with d_{ED} of 6.3 nm at various temperatures corresponding to Fig. 2b. At 500 K, Pd–Pt NPs have five distinct RDF peaks, indicating the regular face center cubic (fcc) structure of the atoms [37–39]. As the temperature increases, Pd atoms start to diffuse along the
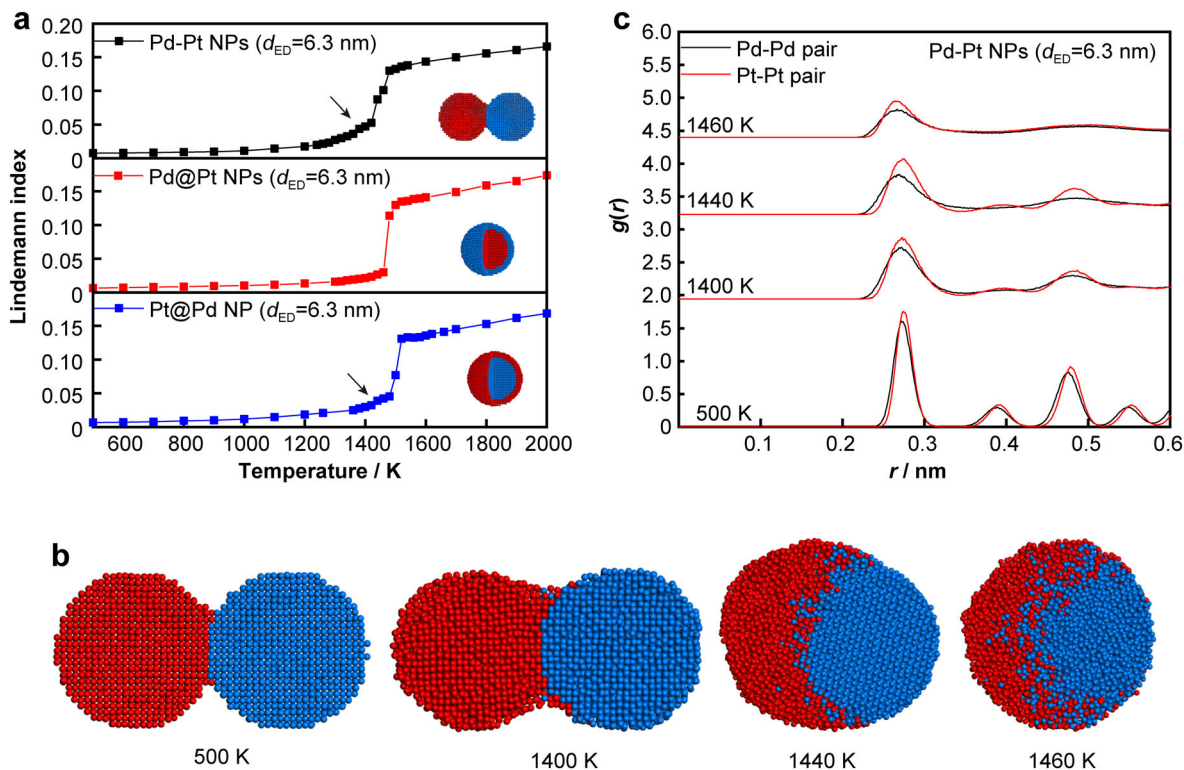

Fig. 2 a Lindemann indices of three types of Pd/Pt bimetallic NPs with d_{ED} or d of 6.3 nm as a function of temperature; b snapshots of cross section of Pd–Pt NPs with d_{ED} of 6.3 nm taken at four representative temperatures, and c RDF of Pd–Pt NPs with d_{ED} of 6.3 nm at various temperatures corresponding to b (coloring denotes atomic type: red, Pd atom; blue, Pt atom)

surface of Pt NP due to the low diffusion barriers [40], similar to the results reported by Nelli et al. [27]. At temperature up to 1400 K, three distinct RDF peaks of Pt–Pt pair and Pd–Pd pair are still obvious and only their heights are reduced, which indicates that most of the atoms are in order. Besides, some initial disordered PdPt alloy regions appear at the interface, while the other surface regions of Pd NP and Pt NP remain unchanged, similar to the melting and coalescence process of Pb–Sb NPs [41]. Thus, the starting temperature of Pd–Pt NPs' melting process is 1400 K. At 1440 K, only the first peak remains in RDF of Pd–Pd pair while all three RDF peaks of Pt–Pt pair remain. This implies that Pd NP has already transformed into liquid and most Pt atoms are still orderly arranged. Meanwhile, more liquid PdPt alloy appears at the interface. At 1460 K, only the first RDF peak of Pt–Pt pair and the first RDF peak of Pd–Pd pair are observed in Pd–Pt NPs, which means the melting of the NPs. Hence, the melting process of Pd–Pt NPs starts at Pd/Pt interface at 1400 K and then develops toward the core of the NPs with increasing temperature, resulting in this process occurring within a broad temperature interval of 60 K. In addition, the disordered interface in Pd–Pt NPs is created by thermal vibration [42]. The atoms on the surface of Pd NP might be migrated from their initial site, and then the Pd point defects are formed. After that, the other atoms, such as the near Pt atoms become unstable because of the decrease in coordination number. The migrated Pd atoms will move to other positions by thermal vibration and collision with other atoms. Meanwhile, the unstable Pt atoms are used to fill the vacancies and form PdPt alloy at the interface. Unlike Pd–Pt NPs, Pd@Pt NP has a clear Pt/Pd interface and ordered atoms (Figs. S1a and S2a). The melting of Pd core and Pt shell occurs simultaneously [24], hence, melting of Pd@Pt NP experiences a narrow temperature range of 20 K.

The Lindemann indices of Pd–Pt NPs with the different d_{ED} in the range of 2.5 to 7.8 nm as a function of the temperature, as displayed in Fig. 3a. The broader Lindemann index rises are observed in Pd–Pt NPs with d_{ED} of 2.5–4.0 nm, while the Lindemann index of Pd–Pt NPs with d_{ED} in the range of 4.8 to 7.8 nm shows similar jumps.

To compare the melting and coalescence mechanisms of Pd–Pt NPs with various d_{ED} during the heating process, the snapshots of the cross section of Pd–Pt NPs with d_{ED} of 2.5 nm taken at four representative temperatures, as shown in Fig. 3b. The RDF of Pd–Pt NPs with d_{ED} of 2.5 nm at various temperatures corresponding to Fig. 3b is exhibited in Fig. 3c. All atoms are ordered below 1060 K according to Fig. 3b, c. At 1060 K, only the first RDF peak of Pd–Pd pair is observed, whereas three RDF peaks of Pt–Pt pair remain, meaning that Pd NP has already transformed into a liquid and Pt NP is in solid form. The second and the third peaks of Pt–Pt pair disappear at 1180 K. This indicates that Pd
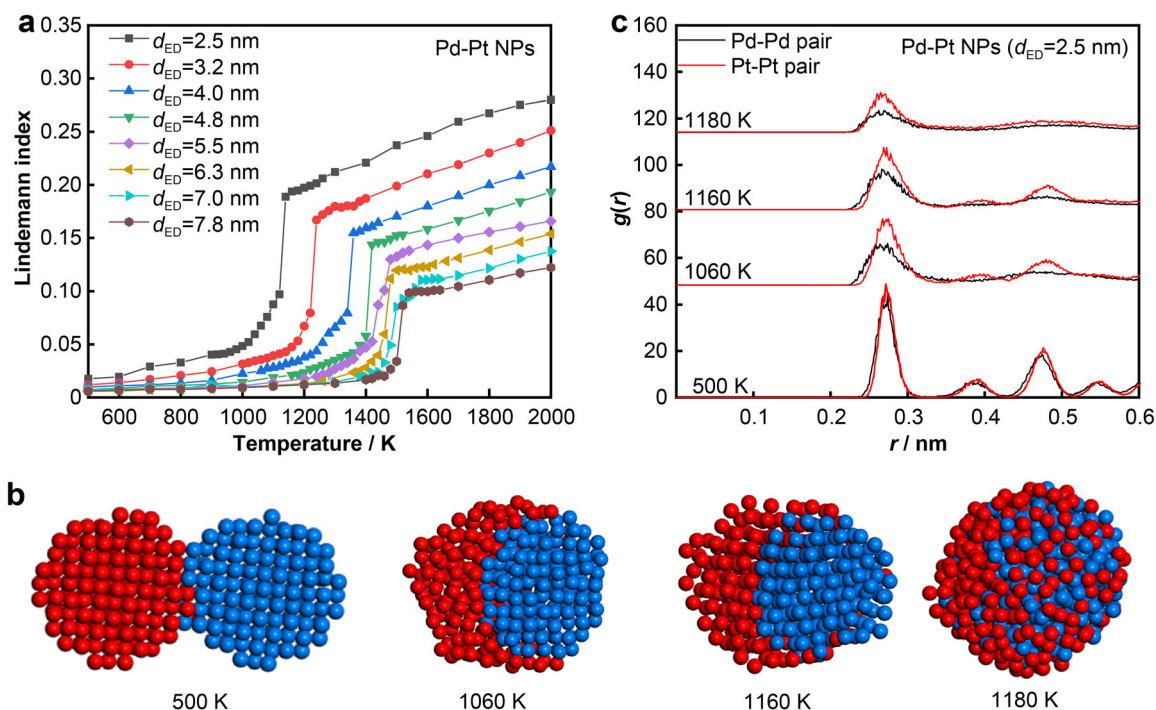

Fig. 3 **a** Lindemann indices of Pd–Pt NPs with different d_{ED} in range of 2.5 to 7.8 nm as a function of temperature; **b** snapshots of cross section of Pd–Pt NPs with d_{ED} of 2.5 nm taken at four representative temperatures and **c** RDF of Pd–Pt NPs with d_{ED} of 2.5 nm at various temperatures corresponding to **b** (coloring denotes atomic type: red, Pd atom; blue, Pt atom)
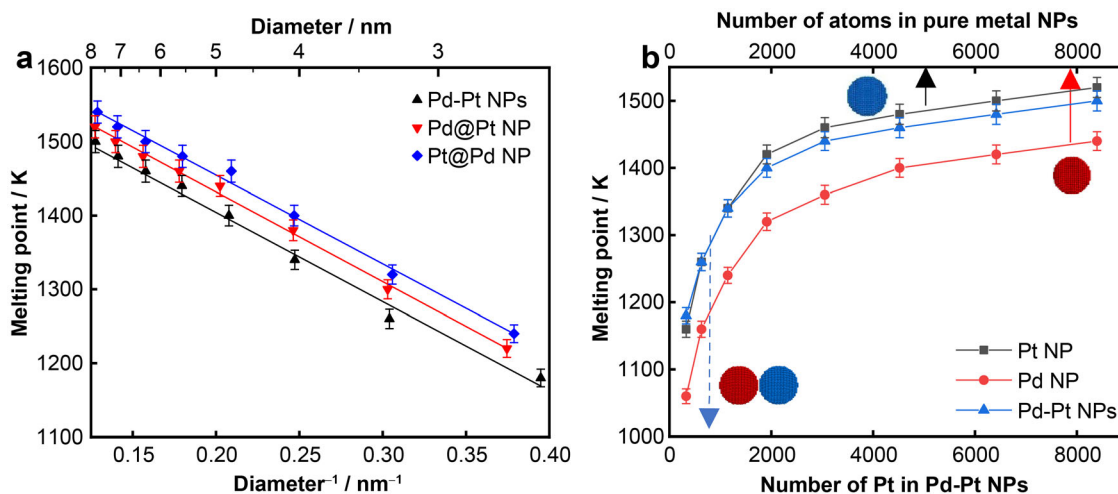
Fig. 4 a Melting points of three types of Pd/Pt bimetallic NPs as a function of inverse of NP diameter, and **b** melting points of pure Pt, pure Pd and Pd–Pt NPs as a function of number of atoms

the melting of Pt NP is independent of the melting of Pd NP in Pd–Pt NPs with d_{ED} of 2.5 nm. The complete melting of Pd–Pt NPs with d_{ED} of 2.5 nm occurs within a broad temperature range of 120 K since Pd NP and Pt NP melt at 1060 and 1180 K, respectively. Besides, the absence of a stable liquid shell on the surface of Pt NP with a small diameter during the melting process is due to the thermal instability of the surface atoms in Pt NP. The crystal morphology of Pt NP changes from an initial sphere to a polyhedron because the specific surface area of a polyhedron is smaller than that of a sphere with the same number of atoms [43], similar to other noble metals [44]. Hence, Pd and Pt diffuse into each other to form liquid PdPt alloy only after Pt NP changes from solid to liquid.

The melting points of the three types of Pd/Pt bimetallic NPs as a function of the inverse of the NP diameter, as depicted in Fig. 4a, where the values of melting points are obtained from their Lindemann index curves (Figs. 3a and S3). For the three types of Pd/Pt bimetallic NPs, there is a negative inverse correlation between the melting point and the inverse of NPs diameter. The melting points of the three types of Pd/Pt bimetallic NPs decrease rapidly as the NP diameter decreases, which indicates a strong diameter dependence of the melting point. Moreover, Pd–Pt NPs possess a lower melting point than the core–shell NPs (Pd@Pt NP and Pt@Pd NP) with the same effective diameter. It is well known that the atoms located in the outer layer play a more important role in the melting process than the inner atoms. Hence, the surface atoms are responsible for the significant decrease in the melting point of Pd–Pt NPs in which the surface atoms are more unstable (Fig. S4).

To explore the relationship of melting point between Pd–Pt NPs and pure noble metal NPs, the melting points as

a function of the number of atoms are shown in Fig. 4b for Pd–Pt NPs, pure Pd NP and pure Pt NP. When the number of Pt atoms in Pd–Pt NPs is the same as that in pure Pt NP, the melting point of Pd–Pt NPs is similar to that of pure Pt NP. In other words, the melting point of Pd–Pt NPs depends on the melting temperature of Pt NP because the melting point of Pt NP is higher than that of Pd NP. These agree well with the discussion about the melting and coalescence process in Pd–Pt NPs (Figs. 2 and 3).

To further investigate the effect of Pt composition on the melting and coalescence mechanisms of Pd–Pt NPs with d_{ED} of 6.3 nm, Pd–Pt NPs with Pt composition in the range of 10 at% to 80 at% were heated. The Lindemann indices of Pd–Pt NPs with the different Pt compositions as a function of the temperature are exhibited in Fig. 5a. A sharp Lindemann index jump is observed for Pd–Pt NPs with Pt composition of 20%, unlike the broad Lindemann index jump of Pd–Pt NPs with the Pt composition of 10 at% and 80 at%. In addition, the dependence of the melting point on the Pt composition is obtained from the Lindemann index curves, as displayed in Fig. 5b. As such, the melting point of Pd–Pt NPs will be determined by the melting temperature of Pt NP, when Pt composition is more than 20 at%. Besides, the melting point of Pd–Pt NPs exhibits an approximately linear increase as Pt composition rises.

To compare the melting and coalescence processes of Pd–Pt NPs with the different Pt compositions, the snapshots of the cross section of Pd–Pt NPs with Pt composition of 10 at% and 20 at% (cited as "Pd-10 at% Pt NPs" and "Pd-20 at% Pt NPs," respectively) taken at several representative temperatures are shown in Fig. 6a, b, respectively. Figure 6c, d shows the RDF of Pd-10 at% Pt NPs and Pd-20 at% Pt NPs at various temperatures
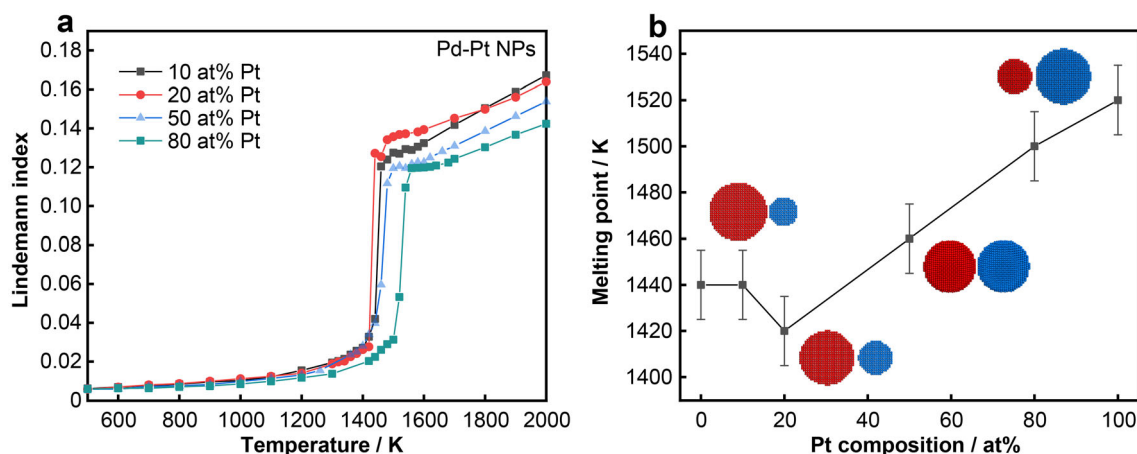
Fig. 5 **a** Lindemann indices of Pd–Pt NPs with different Pt compositions during heating process as a function of temperature, and **b** melting point as a function of Pt composition corresponding to **a**
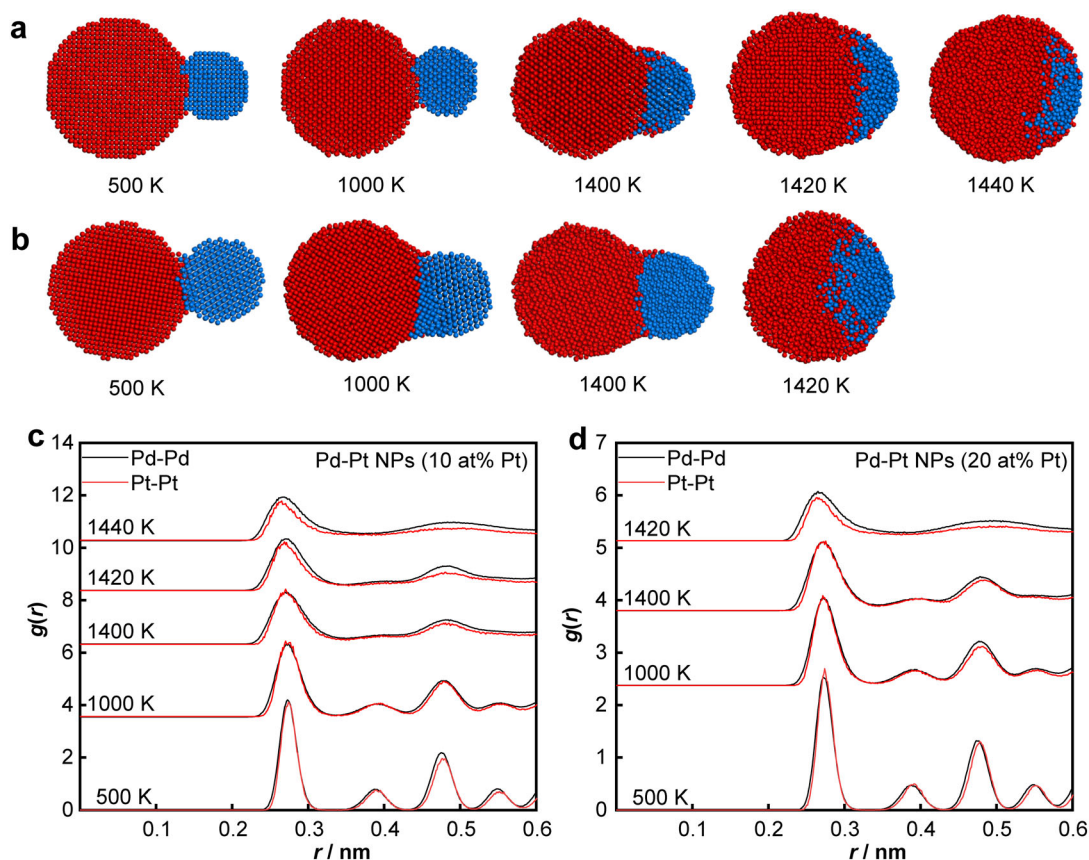

Fig. 6 Snapshots of cross section of Pd–Pt NPs with Pt composition of **a** 10 at% and **b** 20 at% taken at several representative temperatures. RDF of Pd–Pt NPs with Pt composition of **c** 10 at% and **d** 20 at% at various temperatures corresponding to **a** and **b**, respectively (coloring denotes atomic type: red, Pd atom; blue, Pt atom)

corresponding to Fig. 6a, b, respectively. For Pd-10 at% Pt NPs, the morphology of Pt NP changes from an initial sphere to a hemisphere at 1400 K. Three RDF peaks of Pd–Pd pair and three RDF peaks of Pt–Pt pair are observed, meaning a solid–solid transformation mode of the small Pt

NP. At 1420 K, three RDF peaks of Pd–Pd pair and only the first RDF peak of Pt–Pt pair are observed, which indicates that Pt NP has already transformed into a liquid and Pd NP is still in solid form. At 1440 K, only the first RDF peak of Pd–Pd pair appears, implying that Pd NP has

completely melted. Hence, the melting process of Pd–Pt NPs with Pt composition of 10 at% starts from the interface and expands into the interior of the Pd NP. The melting of Pt NP occurs first, followed by Pd NP; since smaller Pt NP has a lower melting temperature. For Pd-20 at% Pt NPs, three RDF peaks of Pt–Pt and three RDF peaks of Pd–Pd pair are still observed at 1400 K, indicating that both Pd NP and Pt NP are orderly arranged. At 1420 K, only the first RDF peaks of Pt–Pt pair and Pd–Pd

pair appear, which means an instantaneous transition of the solid–liquid phase at this temperature. Thus, the melting and coalescence of Pd-20 at% Pt NPs occurs only at a temperature that is similar to the melting temperature of Pt NP and that of Pd NP, experiencing a narrow temperature range. The melting and coalescence of Pd-10 at% Pt NPs is dependent on the melting of Pd NP while that of Pd-20 at% Pt NPs is based on the melting of both Pd and Pt NPs. Since Pd NP in Pd-10 at% Pt NPs melts at a higher temperature
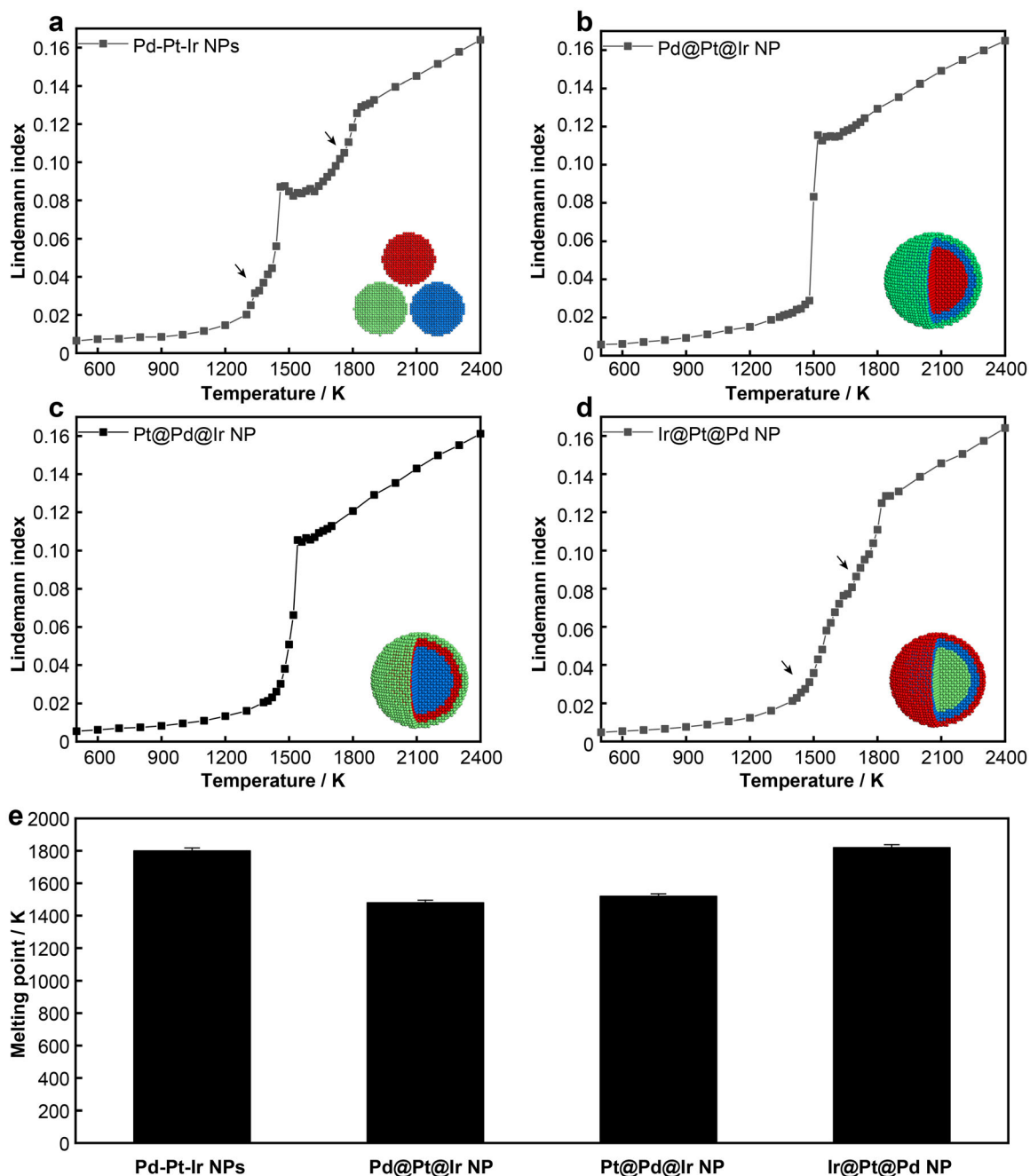

Fig. 7 Lindemann indices of a Pd–Pt–Ir NPs, b Pd@Pt@Ir NP, c Pt@Pd@Ir NP and d Ir@Pt@Pd NP as a function of temperature. e Melting points of four types of Pd/Pt/Ir trimetallic NPs corresponding to a–d

than Pd NP in Pd-20 at% Pt NPs, the melting point of Pd-10 at% Pt NPs is higher than that of Pd-20 at% Pt NPs.

3.2 Melting processes of Pd/Pt/Ir trimetallic NPs

We further investigated the melting behaviors of four types of Pd/Pt/Ir trimetallic NPs. The Lindemann indices of the four types of Pd/Pt/Ir trimetallic NPs as a function of the temperature are displayed in Fig. 7a–d. There are two Lindemann index rises in Pd–Pt–Ir NPs and Ir@Pt@Pd NP (Fig. 7a, b), while only one Lindemann index jump is found for Pd@Pt@Ir NP and Pt@Pd@Ir NP (Fig. 7c, d). In addition, it is found that beyond the first melting transition (1440 K) in Pd–Pt–Ir NPs, the Lindemann index curve exhibits a decrease to a certain extent, unlike the continuously linear rising Lindemann index curve in Ir@Pt@Pd NP. This is mainly attributed to the enhanced diffusion of Pd and Pt atoms in Pd–Pt–Ir NPs after the overall melting, partially lowering the total root-mean-square bond fluctuation of the systems. Moreover, the melting points of four types of Pd/Pt/Ir trimetallic NPs are depicted in Fig. 7e. Pd@Pt@Ir NP has the lowest melting point (1480 K) and the melting point of Ir@Pt@Pd NP is the highest (1820 K).

To further understand the melting and coalescence mechanism of Pd–Pt–Ir NPs during the heating process, the snapshots of the cross section taken at five representative temperatures are displayed in Fig. 8a. The RDF of Pd–Pt–Ir NPs at various temperatures corresponding to Fig. 8a is shown in Fig. 8b. At 500 K, five distinct RDF peaks of Pd–Pd pair, Pt–Pt pair and Ir–Ir pair are observed, indicating the regular fcc structure of the atoms. At 1300 K, only the first RDF peak of Pd–Pd pair and three RDF peaks of Pt–Pt pair and Ir–Ir pair are observed, which means that the Pd NP has become liquid, and Pt and Ir NPs are still solid. Meanwhile, Pd atoms in Pd–Pt–Ir NPs diffuse along the surface of Pt NP and Ir NP, and the portion of Ir and Pt

atoms at Pd/Ir and Pd/Pt interfaces diffuse into the liquid Pd via the thermal vibration mentioned above. At 1440 K, the second and third RDF peaks of Pt–Pt pair disappear, which implies that Pt NP has completely melted. Liquid Pd and Pt diffuse into each other and surround Ir NP because Ir NP is still in solid form. Hence, a meniscus liquid PdPt alloy is formed, unlike spherical liquid PdPt alloy in Pd–Pt NPs. As the temperature rises, the Ir atoms at the interface diffuse into the liquid PdPt area, while the Ir core remains the regular fcc lattice until the melting point of Pd–Pt–Ir NPs. Therefore, the coalescence of Pd–Pt–Ir NPs starts with the melting of Pd NP at 1300 K, followed by Pt NP at 1440 K, then Ir NP at 1800 K, within a broad temperature range of 500 K and a two-step coalescence process. Besides, the melting and coalescence process of Pd–Pt–Ir NPs depends on the melting temperature of Ir NP as Ir NP has the highest melting point.

To investigate the melting mechanisms of Pd@Pt@Ir NP and Pt@Pd@Ir NP, snapshots of their cross section at four representative temperatures are exhibited in Fig. 9. At 1460 K (Fig. 9a), the outermost Ir shell melts and the Ir atoms diffuse into Pt shell for Pd@Pt@Ir NP. At 1480 K, an instantaneous melting of the Pd core occurs. The melting of Pd@Pt@Ir NP occurs within a narrow temperature interval of 20 K from the melting of the outermost Ir shell to Pd core. For Pt@Pd@Ir NP, Pd shell melts, and Pd atoms diffuse into the outermost Ir shell at 1300 K (Fig. 9b). At 1480 K, the liquid IrPd alloy shell forms as well as Ir and Pd atoms diffuse into the solid Pt core. The diffusion process is very fast, and PdPtIr alloy forms at 1520 K. Hence, the melting of Pt@Pd@Ir NP starts from that of Pd shell at 1300 K, and it completely melts at 1520 K, causing a broad temperature range of 220 K. In addition, the melting processes of Pd@Pt@Ir NP and Pt@Pd@Ir NP are different from that of Pd@Pt NP. No interface diffusion occurs in Pd@Pt NP below the melting
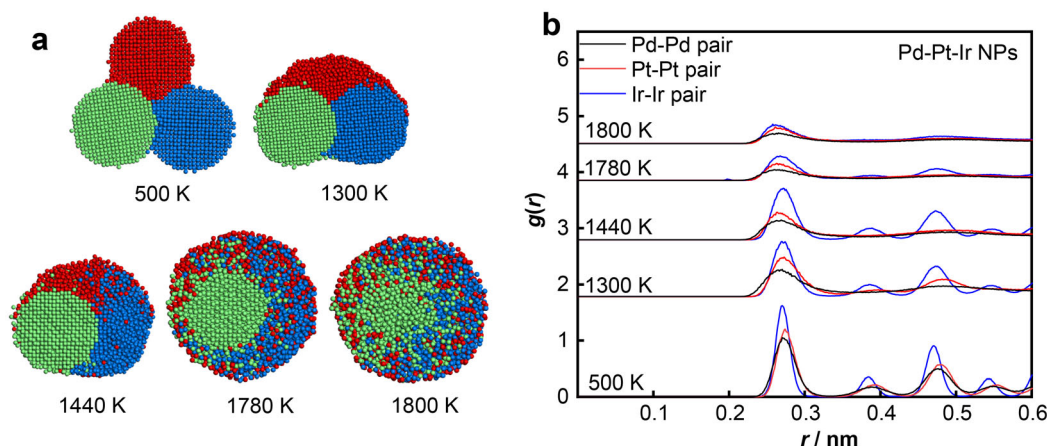

Fig. 8 **a** Snapshots of cross section of Pd–Pt–Ir NPs taken at five representative temperatures, and **b** RDF of Pd–Pt–Ir NPs at various temperatures corresponding to **a** (coloring denotes atomic type: red, Pd atom; blue, Pt atom; green, Ir atom)

point (Fig. S1a). Hence, the melting mechanisms of the Pd/Pt bimetallic NPs are only partially applicable to those of the Pd/Pt/Ir trimetallic NPs.

To understand the melting mechanism of Ir@Pt@Pd NP during the heating process, the snapshots of their cross section taken at five representative temperatures are shown in Fig. 10a. The RDFs of Ir@Pt@Pd NP at various temperatures corresponding to Fig. 10a are displayed in Fig. 10b. The melting process of Ir@Pt@Pd NP begins with the melting of the outermost Pd shell at 1300 K and then develops toward Pt shell and Ir core. At 1700 K, the liquid PdPt alloy shell is formed, and Pd and Pt atoms diffuse into the solid Ir core. Since the melting temperature of Ir core is much higher than 1700 K, Ir core surrounded by a stable liquid shell is still in a perfect lattice state below 1820 K even though the surface of Ir core has melted. Therefore, the melting of Ir@Pt@Pd NP experiences a broad temperature range from the melting of Pd shell at 1300 K to the complete melting of Ir core at 1820 K.
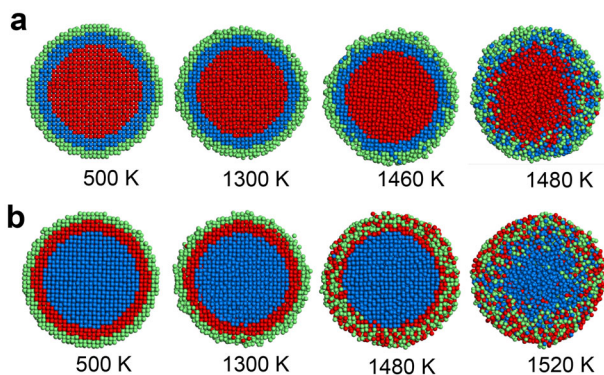
4 Conclusion

By employing the MD simulation, the melting and coalescence mechanisms of Pd–Pt NPs with different effective diameters and compositions were investigated to in-depth understand their structural evolutions during the heating process, and then these were compared to the melting mechanisms of Pd@Pt NP and Pt@Pd NP. For Pd–Pt NPs with an effective diameter of 2.5–4.0 nm, the melting emerged only after both Pd and Pt NP were completely melted. For Pd–Pt NPs with an effective diameter of 4.6–7.8 nm, the melting started at the interface before Pd NP had completely melted and developed toward the interior of the NPs, unlike Pt@Pd NP and Pd@Pt NP possessing the liquid PdPt alloy after Pd portion had completely melted. All atoms except those on Pd/Pt interface remained in the fcc lattice before they had completely melted. Besides, the melting and coalescence process of Pd–Pt NPs was dependent on the melting temperature of Pt NP when the Pt composition was more than 20 at% where Pt NP had a higher melting temperature than Pd one. For Pd–Pt–Ir NPs, the melting started at Pd/Ir, Pd/Pt and Pt/Ir interfaces, and expanded into the interior of NPs, occurring within a broad temperature interval and two-step coalescence process. The coalescence process of Pd–Pt–Ir NPs depended on the melting temperature of Ir portion because its melting temperature was the highest, similar to Ir@Pt@Pd NP. On the contrary, the melting of Pd@Pt@Ir NP and Pt@Pd@Ir NP began from the outmost Ir shell, and PdPtIr alloy was formed after the core melted, experiencing a narrow melting temperature interval. These results show that the spatial distribution of the metals in Pt-based multimetallic spherical NPs can be tailored through precise control of the melting process to control catalytic properties. By understanding how the melting mechanisms are correlated with the structural evolution during the heat-

Fig. 9 Snapshots of cross section of a Pd@Pt@Ir NP and b Pt@Pd@Ir NP taken at four representative temperatures (coloring denotes atomic type: red, Pd atom; blue, Pt atom; green, Ir atom)
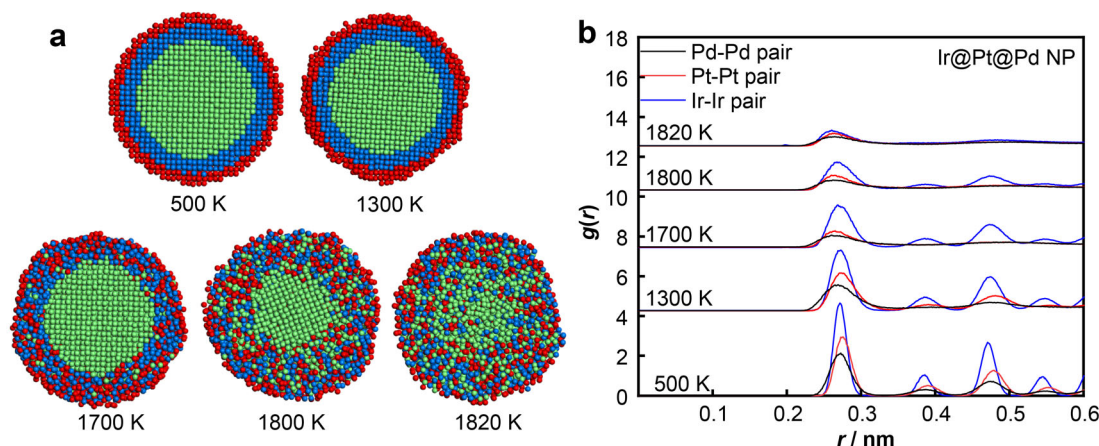

Fig. 10 a Snapshots of cross section of Ir@Pt@Pd NP taken at five representative temperatures, and b RDF of Ir@Pt@Pd NP at various temperatures corresponding to a (coloring denotes atomic type: red, Pd atom; blue, Pt atom; green, Ir atom)

treatment process, we can tailor the experimental Pt-based multimetallic spherical NPs fabrication process, as well as aid in the composition design of these multimetallic alloyed nanocatalysts.

Declarations

Conflict of interests The authors declare that they have no conflict of interest.

References

[1] Wu Z, Caracciolo DT, Maswadeh Y, Wen J, Kong Z, Shan S, Vargas JA, Yan S, Hopkins E, Park K. Alloying realloying enabled high durability for Pt-Pd-3d-transition metal nanoparticle fuel cell catalysts. Nat Commun. 2021;12(1):1. https://doi.org/10.1038/s41467-021-21017-6.

[2] Huang G, Xu ZH, Luo TT, Yan ZX, Zhang M. Fluorescent light enhanced graphitic carbon nitride/ceria with ultra low-content platinum catalyst for oxidative decomposition of formaldehyde at ambient temperature. Rare Met. 2021;40(11):12. https://doi.org/10.1007/s12598-021-01756-7.

[3] Li D, Li Y, Liu X, Guo Y, Pao C, Chen J, Hu Y, Wang Y. NiAl$_2$O$_4$ spinel supported Pt catalyst: high performance and origin in aqueous-phase reforming of methanol. ACS Catal. 2019;9(10):9671. https://doi.org/10.1021/acscatal.9b02243.

[4] Yu J, Zhao H, Chen X, Wei F. Resistive switching characteristics of Pt/Dy$_2$O$_3$/Pt resistive random access memory devices with different rapid thermal annealing process. Chin J Rare Met. 2020;4(12):1286. https://doi.org/10.13373/j.cnki.cjrm.XY16040030.

[5] Lin W. Recovery of high-purity Pt from Pt-Au bimetallic nanoparticles using organic aqua regia. Rare Met. 2012;31(1):92. https://doi.org/10.1007/s12598-012-0469-8.

[6] Yang J, Luo C, He S, Li J, Meng B, Zhang D, Xue Z, Zhou X, Lu X. Synthesis of three-dimensional Au-graphene quantum dots@ Pt core-shell dendritic nanoparticles for enhanced methanol electro-oxidation. Nanotechnology. 2019;30(49):495706. https://doi.org/10.1088/1361-6528/ab3dc3.

[7] Malankowska A, Kobylanski MP, Mikolajczyk A, Cavdar O, Nowaczyk G, Jarek M, Lisowski W, Michalska M, Kowalska E, Ohtani B. TiO$_2$ and NaTaO$_3$ decorated by trimetallic Au/Pd/Pt core-shell nanoparticles as efficient photocatalysts: experimental and computational studies. ACS Sustain Chem Eng. 2018;6(12):16665. https://doi.org/10.1021/acssuschemeng.8b03919.

[8] Chen J, Niu Q, Chen G, Nie J, Ma G. Electrooxidation of methanol on Pt@Ni bimetallic catalyst supported on porous carbon nanofibers. J Phys Chem C. 2017;121(3):1463. https://doi.org/10.1021/acs.jpcc.6b10882.

[9] Zhang J, Chen T, Yao P, Jiao Y, Wang J, Chen Y, Zhu Q, Li X. Catalytic cracking of n-decane over monometallic and bimetallic Pt-Ni/MoO$_3$/La-Al$_2$O$_3$ catalysts: correlations of surface properties and catalytic behaviors. Ind Eng Chem Res. 2019;58(5):1823. https://doi.org/10.1021/acs.iecr.8b04712.

[10] Zhang Y, Zhang J, Chen Z, Liu Y, Zhang M, Han X, Zhong C, Hu W, Deng Y. One-step synthesis of the PdPt bimetallic nanodendrites with controllable composition for methanol oxidation

[11] Ramachandran RK, Dendooven J, Detavernier C. Controlled synthesis of Fe-Pt nanoalloys using atomic layer deposition. Nanotechnology. 2020;32(9):95602. https://doi.org/10.1088/1361-6528/abc5f5.

[12] Luo Q, Wang S, Zhu Y, Tang S, Du Y. Structurally ordered Pt$_3$Co for oxygen reduction reaction prepared using polyvinylpyrrolidone as auxiliary dispersant. Nanotechnology. 2020;31(45):455605. https://doi.org/10.1088/1361-6528/ababc9.

[13] Yao K, Zhao C, Wang N, Li T, Lu W, Wang J. An aqueous synthesis of porous PtPd nanoparticles with reversed bimetallic structures for highly efficient hydrogen generation from ammonia borane hydrolysis. Nanoscale. 2020;12(2):638. https://doi.org/10.1039/C9NR07144J.

[14] Goodman ED, Dai S, Yang A, Wrasman CJ, Gallo A, Bare SR, Hoffman AS, Jaramillo TF, Graham GW, Pan X. Uniform Pt/Pd bimetallic nanocrystals demonstrate platinum effect on palladium methane combustion activity and stability. ACS Catal. 2017;7(7):4372. https://doi.org/10.1021/acscatal.7b00393.

[15] Hao R, Feng QL, Wang XJ, Zhang YC, Li KS. Morphology-controlled growth of large-area PtSe$_2$ films for enhanced hydrogen evolution reaction. Rare Met. 2022;41(4):1314. https://doi.org/10.1007/s12598-021-01877-z.

[16] Tayal A, Seo O, Kim J, Kobayashi H, Yamamoto T, Matsumura S, Kitagawa H, Sakata O. Mechanism of hydrogen storage and structural transformation in bimetallic Pd-Pt nanoparticles. ACS Appl Mater Inter. 2021;13:23502. https://doi.org/10.1021/acsami.0c22432.

[17] Çögenli MS, Yurtcan AB. Catalytic activity, stability and impedance behavior of PtRu/C, PtPd/C and PtSn/C bimetallic catalysts toward methanol and formic acid oxidation. Int J Hydrog Energy. 2018;43(23):10698. https://doi.org/10.1016/j.ijhydene.2018.01.081.

[18] Lim B, Jiang M, Camargo PH, Cho EC, Tao J, Lu X, Zhu Y, Xia Y. Pd-Pt bimetallic nanodendrites with high activity for oxygen reduction. Science. 2009;324(5932):1302. https://doi.org/10.1002/chin.200933011.

[19] Da Silva AG, Fernandes CG, Hood ZD, Peng R, Wu Z, Dourado AH, Parreira LS, de Oliveira DC, Camargo PH, de Torresi SIC. PdPt-TiO$_2$ nanowires: correlating composition, electronic effects and O-vacancies with activities towards water splitting and oxygen reduction. Appl Catal B Environ. 2020;277: 119177. https://doi.org/10.1016/j.apcatb.2020.119177.

[20] Cao K, Zhu Q, Shan B, Chen R. Controlled synthesis of Pd/Pt core shell nanoparticles using area-selective atomic layer deposition. Sci Rep. 2015;5(1):1. https://doi.org/10.1038/srep08470.

[21] Xiao X, Jeong H, Song J, Ahn J, Kim J, Yu T. Facile synthesis of Pd@Pt core-shell nanocubes with low Pt content via direct seed-mediated growth and their enhanced activity for formic acid oxidation. Chem Commun. 2019;55(79):11952. https://doi.org/10.1039/C9CC05915F.

[22] Nelli D, Krishnadas A, Ferrando R, Minnai C. One-step growth of core-shell (PtPd)@Pt and (PtPd)@ Pd nanoparticles in the gas phase. J Phys Chem C. 2020;124(26):14338. https://doi.org/10.1021/acs.jpcc.0c02621.

[23] Lin X, Wang A, Fang K, Yuan J, Feng J. One-pot seedless aqueous synthesis of reduced graphene oxide (rGO)-supported core-shell Pt@Pd nanoflowers as advanced catalysts for oxygen reduction and hydrogen evolution. ACS Sustain Chem Eng. 2017;5(10):8675. https://doi.org/10.1021/acssuschemeng.7b01400.

[24] Huang R, Wen Y, Zhu Z, Sun S. Pt-Pd bimetallic catalysts: structural and thermal stabilities of core-shell and alloyed

nanoparticles. J Phys Chem C. 2012;116(15):8664. https://doi.org/10.1021/jp3015639.

[25] Huang R, Wen Y, Zhu Z, Sun S. Two-stage melting in core-shell nanoparticles: an atomic-scale perspective. J Phys Chem C. 2012;116(21):11837. https://doi.org/10.1021/jp303877u.

[26] Li Y, Qi W, Huang B, Ji W, Wang M. Size-and composition-dependent structural stability of core-shell and alloy Pd-Pt and Au-Ag nanoparticles. J Phys Chem C. 2013;117(29):15394. https://doi.org/10.1021/jp404422y.

[27] Nelli D, Cerbelaud M, Ferrando R, Minnai C. Tuning the coalescence degree in the growth of Pt-Pd nanoalloys. Nanoscale Adv. 2021;3:836. https://doi.org/10.1039/D0NA00891E.

[28] Guo S, Dong S, Wang E. Three-dimensional Pt-on-Pd bimetallic nanodendrites supported on graphene nanosheet: facile synthesis and used as an advanced nanoelectrocatalyst for methanol oxidation. ACS Nano. 2010;4(1):547. https://doi.org/10.1021/nn9014483.

[29] Wang D, Li Y. Bimetallic nanocrystals: liquid-phase synthesis and catalytic applications. Adv Mater. 2011;23(9):1044. https://doi.org/10.1002/adma.201003695.

[30] Zhu J, Xie M, Chen Z, Lyu Z, Chi M, Jin W, Xia Y. Pt-Ir-Pd trimetallic nanocages as a dual catalyst for efficient oxygen reduction and evolution reactions in acidic media. Adv Energy Mater. 2020;10(16):1904114. https://doi.org/10.1002/aenm.201904114.

[31] Plimpton S. Fast parallel algorithms for short-range molecular dynamics. J Comput Phys. 1995;117(1):1. https://doi.org/10.1006/jcph.1995.1039.

[32] Plimpton SJ, Thompson AP. Computational aspects of many-body potentials. MRS Bull. 2012;37(5):513. https://doi.org/10.1557/mrs.2012.96.

[33] Sheng HW, Kramer MJ, Cadien A, Fujita T, Chen MW. Highly optimized embedded-atom-method potentials for fourteen fcc metals. Phys Rev B. 2011;83(13):134118. https://doi.org/10.1103/physrevb.83.134118.

[34] Johnson RA. Alloy models with the embedded-atom method. Phys Rev B. 1989;39(17):12554. https://doi.org/10.1103/PhysRevB.39.12554.

[35] Zhou Y, Karplus M, Ball KD, Berry RS. The distance fluctuation criterion for melting: comparison of square-well and Morse potential models for clusters and homopolymers. J Chem Phys. 2002;116(5):2323. https://doi.org/10.1063/1.1426419.

[36] Khalkhali M, Liu Q, Zeng H, Zhang H. A size-dependent structural evolution of ZnS nanoparticles. Sci Rep. 2015;5(1):1. https://doi.org/10.1038/srep14267.

[37] Akbarzadeh H, Mehrjouei E, Ramezanzadeh S, Izanloo C. Ni-Co bimetallic nanoparticles with core-shell, alloyed, and Janus structures explored by MD simulation. J Mol Liq. 2017;248:1078. https://doi.org/10.1016/j.molliq.2017.10.135.

[38] Celtek M, Sengul S, Domekeli U. Glass formation and structural properties of $Zr_{50}Cu_{50-x}Al_x$ bulk metallic glasses investigated by molecular dynamics simulations. Intermetallics. 2017;84:62. https://doi.org/10.1016/j.intermet.2017.01.001.

[39] Van Hoang V. Molecular dynamics simulation of liquid and amorphous Fe nanoparticles. Nanotechnology. 2009;20(29):295703. https://doi.org/10.1088/0957-4484/20/29/295703.

[40] Vej-Hansen UG, Rossmeisl J, Stephens IE, Schiøtz J. Correlation between diffusion barriers and alloying energy in binary alloys. Phys Chem Chem Phys. 2016;18(4):3302. https://doi.org/10.1039/c5cp04694g.

[41] Devi MM, Tiwari K, Biswas K. Size-dependent melting behavior of Pb-17.5 at. pct Sb-free biphasic alloy nanoparticles. Metall Mater Trans A. 2019;50:3959. https://doi.org/10.1007/s11661-019-05275-0.

[42] Van Der Veen JF. Melting and freezing at surfaces. Surf Sci. 1999;433:1. https://doi.org/10.1016/S0039-6028(99)00084-9.

[43] Liang T, Zhou D, Wu Z, Shi P. Size-dependent melting modes and behaviors of Ag nanoparticles: a molecular dynamics study. Nanotechnology. 2017;28(48):485704. https://doi.org/10.1088/1361-6528/aa92ac.

[44] Taherkhani F, Akbarzadeh H, Feyzi M, Rafiee HR. Disorder effect on heat capacity, self-diffusion coefficient, and choosing best potential model for melting temperature, in gold-copper bimetallic nanocluster with 55 atoms. J Nanopart Res. 2015;17(1):1. https://doi.org/10.1007/s11051-015-2860-5.